Green synthesis of germanium nano ink and inkjet printing of Si/Ge heterostructure

Hemaprabha Elangovan[a], *Ankita Maske*[b], *Ravishankar Narayanan*[c], *Praveen C Ramamurthy*[a,c], *Kamanio Chattopadhyay*[a,c*]

[a]Interdisciplinary Centre for Energy Research, Indian Institute of Science, Bangalore 560012, India.
[b]Materials Research Centre, Indian Institute of Science, Bangalore 560012, India.
[c]Department of Materials Engineering, Indian Institute of Science, Bangalore 560012, India.

Corresponding author email: *kamanio@iisc.ac.in*

Abstract

We present a green route of synthesis of germanium nanocrystals by cryomilling. The particles (~ 80 nm) are further functionalized with acrylic acid and dispersed in the isopropyl alcohol (IPA) medium to obtain colloidal ink suitable for inkjet printing under ambient atmosphere to form device grade structure. Printing on silicon wafers presents a complex problem of coffee-ring pattern formation that hinders the printing quality. Enhancing the printing quality can be realized by controlling the hydrophobicity of the silicon surface by optimizing termination of the surface bond through a cleaning protocol and temperature of printing. Through a simple model architecture using n-type Si (001) substrate, the diode performance of the Si/Ge printed heterostructure that has the potential to evolve into a cost-effective development of semiconducting devices is demonstrated.

Keywords: cryomilling; nanocrystalline; functionalization; coffee-ring; inkjet printing.

1 Introduction

Silicon-germanium (Si/Ge) heterojunctions are useful in many applications such as solar cells [1, 2], photodetectors [3, 4], bipolar transistors [5, 6], field-effect transistors [7-9], thermoelectrics [10-12] and many others [13]. Hence, continuing efforts are underway to obtain less expensive methods of fabrication of silicon-germanium heterostructures. In this regard, inkjet printing technique of device fabrication under ambient condition is attractive as this is a direct patterning process. The method also can eliminate the need for special vacuum technologies and clean room, making it attractive in the context of the development of a low-cost, low-capital technology [14].

The nature and the quality of ink containing the materials needed for the device are critical for inkjet printing. In most cases, this ink is composed of dispersed nanoparticles [15-17]. For the fabrication of Si/Ge heterojunctions, a pre-requisite is the germanium ink, which necessitates the need for germanium nanoparticles. Various methods have been employed in synthesizing germanium nanoparticles such as gas decomposition [18], chemical route of reducing Ge salts [19, 20], laser synthesis [21] and thermolysis [22]. The chemical route is the most popular for the synthesis of nanoparticles. However, the disposal of the chemical residue presents an environmental challenge, thus encouraging the development of chemical-free green processes. In this work, germanium nanoparticles have been fabricated by the technique of milling at low temperature (cryomilling) under an inert atmosphere that is relatively inexpensive and scalable. The common issue of contamination during conventional planetary ball milling can be overcome during cryomilling [23]. Lower milling temperature (~200 K) and the inert atmosphere (argon) maintained during milling helps in overcoming the problem due to poor stability of germanium

in air [24]. This method also results in germanium nanoparticles without any by-product, making this a clean way for nanoparticle synthesis.

Large research efforts exist in the area of printable metal contacts for devices [25], polymer [26-28] and ceramic printing [29, 30]. However, printing elemental semiconductors presents an additional challenge as oxidation of these materials complicates the process. In this work, the use of inkjet printing technique in obtaining germanium film using colloidal germanium obtained from the milling and investigation of the behavior of Si/Ge heterojunction obtained by printing is explored. To the best of our knowledge, this is the first report on inkjet printed germanium films. The key parameters that lead to the formation of device quality films will be discussed in detail.

2 Experimental Section

2.1 Materials

Germanium pellets of 99.9999% purity and intrinsic in nature were purchased from Zhongnuo Advanced Material (Beijing) Technology Co. Ltd with **a** diameter of 2-5 mm. These were used without any further modifications for cryomilling. HF (48%, SDFCL), HNO_3 (69 vol% Emplura), IPA (Fisher Scientific), DI water were also used without any further purification.

2.2 Cryomilling

A specially designed vibratory cryomill capable of milling under vacuum/inert atmosphere was used [24]. The schematic of the mill is given in supplementary Figure S1. The mill was loaded with 5 gm germanium pellets and 500 gm steel ball, giving the ball to powder weight ratio of 100:1. The vial was evacuated with up to 0.02 mbar. The pellets were milled for 5 hours to obtain flakes of germanium particles. The cryomill was maintained at a temperature of ~200 K by a continuous supply of liquid nitrogen through an insulated outer jacket.

2.3 Surface functionalization of germanium nanoparticles

Germanium nanoparticles (~300 mg) obtained through cryo milling are dispersed in methanol medium and subsequently centrifuged for 5 minutes at 5000 rpm. The centrifuged particles are etched with 2% HF. The etched particles are further dispersed in 20 ml acrylic acid and heated for 1 hour at 80 °C. The reaction is carried out under N_2 atmosphere. After the completion of the reaction, the solution is centrifuged again for 10 minutes at 10,000 rpm. Excess acrylic acid is discarded, and the settled particles were collected. These particles were washed repeatedly with methanol to remove excess acrylic acid. The particles were then dispersed in IPA for making ink for printing.

2.4 The process of printing

A (001) orientation phosphorous doped n-type Si wafer of resistivity 1-10 ohms is used throughout this work. Wafer cleaning procedure has been followed as follows: Si wafer is ultrasonically cleaned in acetone for 10 minutes. However, this step leaves the residues due to the solvent itself. This is removed by sonication in methanol/ethanol for 2-5 minutes. This step removes organic and oily residues from the substrate surface. The sample is then cleaned by DI water and dried using N_2 gas. The wafer is then soaked in a 4:1 mixture of H_2SO_4 and H_2O_2 at 90 °C for 10 minutes to remove organic residues. Subsequently, wafer is soaked in a 5:1:1 mixture of DI water + H_2O_2 and HCl at 75 °C for 10 minutes. This procedure eliminates the remaining traces of metal (ionic) contaminants from the wafer. It also forms a thin passivizing layer on the wafer surface, which protects the surface from further contamination. This process is termed as 'RCA cleaning' [31]. For certain experiments, Si wafer is dipped in 2% HF for 2 minutes to remove the oxide layer that forms in the prior cleaning process.

Microfab Jetlab-4 tabletop inkjet printer was used for printing [32]. A piezoelectric print nozzle with the opening of 50 µm size was used. Experiments were carried out with on-the-fly mode with a print speed of 5 mm/sec. For the ink, the germanium concentration was varied from 20 mg/ml to 80 mg/ml of solvent before an optimum value of 40 mg/ml of IPA is determined. The voltage conditions were optimized to obtain the desired drop formation. The ink was stable for about 30 min. Further, a magnetic stirrer that comes in-built with the printing setup was used to avoid particles from settling down while printing. The substrate was placed on the stage, and the temperature was varied between room temperature to 100 °C. Germanium ink was printed as 5x5 mm patch on 10 x10 mm Si substrate. Sintering of the samples was performed in a vacuum furnace maintained at a pressure of 10^{-5} bar.

2.5 Characterization

X-Ray Diffraction (XRD) studies were performed using a PANalytical x-ray diffractometer with a Cu-Kα (1.54 Å) source (operated at 40 kV with a current of 40 mA). Transmission Electron Microscope (TEM) study was performed using a Tecnai T20 microscope at 200 kV equipped with a LaB_6 thermionic emission gun. TEM samples were prepared by drop-casting the germanium nanoparticles dispersion on carbon-coated copper grids and used after solvent evaporation. A Sirion Scanning Electron Microscope (FEI make) was used for imaging. Raman spectra were obtained using LabRam HR Raman spectrometer with a green laser operating at a wavelength of 532 nm. FTIR measurements on nanoparticles were carried out at room temperature using a Perkin Elmer Frontier MIR system. An average of 64 scans was acquired at a spectral resolution of 2 cm^{-1}. Keithley 4200SCS apparatus was used for current-voltage (I-V) measurements.

3 RESULTS AND DISCUSSION

3.1 Cryomilling of germanium and structural characterization

Germanium pellets were cryomilled for 5 hours and XRD analysis was carried out on the powder. Most of the XRD peaks (Figure. 1) could be matched with the diamond cubic structure of germanium with a lattice parameter of a=0.5666 nm slightly higher than the reported value of 0.5658 nm. This, we believe, is due to either error in instrument calibration or possible milling induced contamination. The XRD pattern is obtained from the as-milled powder that contains a large fraction of micron size particles and hence, the peaks are relatively sharper with very weak overlapping broad peaks. **We note that the phase and hence peak positions do not change while the size do changes with relatively small fraction of very fine nanoparticles that can lead to broadening. Therefore, to perform deconvolution, the choice of the two peak position were kept the same and the deconvolution was performed using a log-normal fit. The peak broadening (full width at half maximum (FWHM)) obtained from the broad peak corresponding to the finer crystals was used for crystallite size calculation employing the Scherrer equation.** The inset in Figure. 1 shows deconvolution of the 111 peak. The particle size estimated from the broad peak is of the order of ~50 nm. The milled particles are centrifuged to separate the finer particles. Additional peaks corresponding to germanium oxide with hexagonal structure has also been observed. Comparing the intensity of germanium and germanium oxide reflections, the relative amount of the oxide is found to be 3.9%, suggesting that the particles may have oxide cover.

Cryomilled germanium powder in methanol was centrifuged to get rid of the larger particles and the particles in the supernatant liquid have been analyzed using TEM. Figure 2a shows a TEM bright field micrograph exhibiting the particles. The diffraction pattern (inset of Figure. 2a)

shows the rings corresponding to the diamond cubic crystal structure of nanocrystalline germanium. A histogram of the size distribution (shown in the inset) reveals the mode at 80 nm. As can be seen in the higher magnification image of a particle, nanocrystals are embedded in this particle. High-resolution TEM image (Figure. 2b) also confirms the presence of crystallites of the nanometric size range. This is in accordance with the data obtained from Raman spectroscopy. These results show that the germanium nanoparticles obtained from cryomilling are polycrystalline in nature.

3.2 Synthesis of germanium ink

XRD results showed that the germanium nanoparticles contain trace amounts of germanium oxide, which is expected as germanium is prone to oxidation. However, for printing applications germanium oxide layer can act as an insulating medium. Hence, the surface termination of functional groups has been carried out to suppress oxides in the germanium surface as well as to enhance colloidal stability. Size of the Ge NPs is in the range of ~80 nm, which requires a strong functional termination and for the present range, acrylic acid has been proved effective by Bywalez et al. [40]. It should be noted that the functionalization process is performed to alter the surface termination of the nanoparticles and do not change the size of the particles. Hence, acrylic acid has been used to functionalize germanium. Identity of surface species on germanium nanoparticles is confirmed by comparing the FTIR spectra of as-milled germanium nanoparticles, acrylic acid treated germanium nanoparticles and acrylic acid (Figure. 3a). The peaks present at 2853 – 2962 cm^{-1} are assigned to C-H symmetric and asymmetric stretching in a saturated hydrocarbon (SP_3 C-H) respectively [41, 42]. The absorption at 1610 cm^{-1} indicates the presence of C=C. This absorption is absent in functionalized germanium. Thus, from the presence of sp^3 C-H absorption band and absence of C=C it can be concluded that the Ge-C

functionalization has occurred through the breaking of doubly bonded carbon atoms. The peaks observed at 1400 and 1410 cm^{-1} are attributed to COO- [43, 44]. Additional stretches located in the range 1260-1150 cm^{-1} can be assigned to the coupled C-(OH) stretching and C-O-H bending modes [44]. The stretches at 1465 cm^{-1} and 1260 cm^{-1} are assigned to the scissoring and bending of Ge-C and Ge-CH_2 bonds respectively [41]. The choice of 1450 cm^{-1} is ambiguous because the strong C-CH_x signal appears in the same range and overlaps with Ge-C signal. However, the bending vibration at 1260 cm^{-1} further confirms the presence of Ge-C. The presence of stretch at 860 cm^{-1} is also attributed to Ge-C [45]. Hence, the spectrum shows features consistent with the germanium surface functionalized by propionic acid. The magnified FTIR spectra in the lower wavenumber range are shown in Figure. 3b. This shows the characteristic Ge-O stretches at 800 – 950 cm-1[43, 46]. These are negligible in the functionalized germanium nanoparticles, which shows that the process of hydrogermylation followed by functionalization has resulted in the removal of germanium surface oxide [40]. The oxide amount can be considered insignificant since it is known that FTIR is more sensitive to polar Ge-O than Ge-C stretches. Thus, termination by propionic acid prevents oxidation of the particles and creates a stable passivation layer.

Propionic acid terminated germanium nanoparticles can be dispersed easily in any polar solvent, as the functional group is hydrophilic [47]. The functionalized germanium nanoparticles are found to be stable for about half an hour and this colloidal germanium have been further used for inkjet printing. A built-in magnetic stirrer attached to the colloid reservoir aids in getting a stable colloid throughout the printing.

3.3 Printing of germanium ink and overcoming coffee-ring formation

The inkjet printing method of deposition utilizes inks made of dispersed/dissolved particles, as the source of deposition. The colloid filled reservoirs are connected to a piezoelectric responsive nozzle, from which the drops are ejected. The ejected drop falls on the substrate and when the solvent dries, the film is obtained. When a drop dries on a substrate, it leaves a thick deposit of solute along its periphery. This phenomenon is called coffee-ring formation [48]. This happens because of the non-uniform drying of the drop. In case of solution-processing technique like inkjet printing. This effect hinders the formation of uniform and homogeneous coating. This results in large differences in the thickness and consequent sintering characteristics of the particles that deteriorate the transport properties. Hence, overcoming this effect is necessary for fabricating device quality films. Hence, several experiments have been performed to optimize the concentration of the colloid, nature of the solvent, substrate type, substrate temperature and printing parameters.

Functionalized germanium nanoparticles dispersed in methanol is used for inkjet printing experiments. Methanol was chosen as the solvent since it has a low boiling point and hence the evaporation of the solvent can be achieved at lower substrate temperature compared to the polar solvents such as water. However, the drop formation is not stable and satellites formation (stretching of drops) is observed after a few printing runs [17]. This might be due to low solvent viscosity. Based on the observations, Isopropyl alcohol (IPA) is chosen as a subsequent solvent in order to get stable a drop since its viscosity (2.04 cP) is ~4 times than that of methanol (0.54 cP). Stable drop formation could be observed under this condition.

Initial printing experiments were carried out both on hydrophilic and hydrophobic Si substrates. The hydrophilic surface is obtained by the process of RCA cleaning (detailed in the experiment section). This step creates an ultrathin SiO2 layer in the substrate (~2 nm) and the oxide-

terminated silicon wafer becomes hydrophilic. Hydrophobic substrates were obtained by immersing Si substrates in 2% HF for 2 minutes. This step created hydride terminated silicon surface aiding in hydrophobicity of silicon surface. This is shown as a schematic in Figure. 4a.

It is observed from Figure. 4b that the tendency to form coffee-ring is prominent in the case of the hydrophilic substrate surface. Since, the polar solvent is used, the drop tends to spread on the hydrophilic substrate. This leads to an increase in the ring size. Shen et al. studied the effect of droplet size on the morphology and concluded that the morphology is more uniform for small drops [49]. The solvent evaporation and solute diffusion are two competing factors that determine the drop morphology. In smaller drops, the difference in evaporation rate between the periphery and center decreases, hence the solvent evaporates faster. As a result, there is not enough time available for solute diffusion leading to uniform morphology. In the case of the hydrophilic substrate, drop spreads and becomes larger leading to coffee ring formation. Hence, hydrophobic surfaces were opted for further experiments.

In order to arrest the solute diffusion and to aid the faster evaporation of the solvent, the substrate temperature was increased. The morphology of the drops printed on hydrophobic surface at two different temperatures is shown in Figure. 4c and d. It can be observed that the coffee-ring effect is predominant at high temperature (100 °C) than at room temperature. A similar effect on substrate temperature has been observed by Soltman et al. where the ring effect is avoided by using cooled substrates [50]. The effect of the high temperature resulting in a coffee ring is explained based on the capillary flow [51]. Schematic of the capillary flow is shown in Figure. 4e. When the drop is on the substrate surface, the solvent in the edge of the drop surface dries faster than in the center. This pins the periphery of the drop and forms a contact line. When the solvent in the edge dries faster, excess solvent from the central region flows to the outside to

compensate the solvent loss. This flow carries the solute towards the periphery resulting in a ring like morphology. This effect can be suppressed by performing printing at lower temperatures, as observed in Figure. 4d.

Printing on the hydrophobic substrate at room temperature showed the best printing morphology with no presence of rings. Having optimized the parameters, the germanium ink was printed on silicon substrate for several runs in this condition to get dense film and further experiments were carried out with these samples.

3.4 Sintering of the inkjet printed germanium film

The as-printed films possess separated particles and a continuous network is necessary for the charge transport. This can be achieved by the sintering process. The functional group can act as an insulating layer for the charge carriers. This sintering step also gets rid of the functional group on the particle surface. To identify the decomposition of propionic acid groups from the germanium surface, the functionalized particles were dried and then subjected to thermogravimetric analysis (TGA), under argon atmosphere. A slow weight loss of 0.52% is observed till 400 °C, which is attributed to the decomposition of propionic moieties from the Ge surface. Therefore, the temperatures higher than 400 °C have been chosen for sintering. The printed films were sintered at 600 °C and 800 °C under vacuum. The morphology of the as printed films (Figure. 5a) depicts the individual particles. Morphology of the film sintered at 600 °C (Figure. 5b) shows the onset of sintering. When the sintering temperature is further increased to 800 °C, uniform morphology could be observed. This is expected because of the early melting of the smaller particles in the large size distribution of the nanoparticles and this liquid phase sintering promotes a relatively homogeneous film, as shown in Figure. 5c [52, 53].

Raman spectroscopy has been performed on the films sintered at different temperatures and the spectra are shown in Figure. 5d. Crystalline Si (c-Si) and crystalline-Ge (c-Ge) exhibit the active phonon mode at a frequency of 521 cm-1 and 301.5 cm-1 respectively [54]. For bulk Ge, the spectrum shows a single sharp symmetric peak at 301 cm-1 with a width of approximately 3.9 cm-1 (Figure S2). This peak corresponds to the active phonon mode of crystalline Ge (c-Ge) [33]. For milled powder, this peak shifted to a lower wavenumber of 296 cm^{-1} and asymmetrically broadened with FWHM of 16.9 cm^{-1} (Figure S2). The phonon confinement model [34], states that the peak shift towards left and broadening occur as the crystallite size decreases. The asymmetrical peak broadening towards lower wavenumber suggest coexistence of amorphous and crystalline phase [35-39]. Unlike as-milled germanium powder, Raman spectrum for Ge/Si sintered sample does not show asymmetrical broadening at lower wavenumbers, which marks the absence of amorphous Ge phase. This is expected as crystallization in Ge tends to occur at such high temperatures. The Raman spectrum for the sample sintered at 600 °C shows the peaks for c-Si and c-Ge. The peak at 450 cm^{-1}, seen in the sample sintered at 800 °C corresponds to Ge-Si bond indicative of the presence of Si-Ge alloy at the heterostructure interface. For the as milled Ge, the peak occurs at ~295 cm^{-1} while for a sintered sample at 800 °C, a peak appears at 299 cm^{-1}, indicating the crystallite growth during sintering. Additionally, the shift of the peak to higher wavenumber indicates strain relaxation that is expected at high temperature. A small peak appearing at 450 cm^{-1} corresponds to Ge-Si bond. The oxide peaks are not present in the as-deposited (printed) Ge on Si or in the sintered sample. This shows that the acrylic ligands attached to the germanium protect the samples from the oxidation during and after the printing process.

3.5 Charge transport in Si/Ge heterojunction

The thickness of germanium film printed on Si substrate is measured to be ~5 µm. To perform current-voltage measurements, silver metal contacts have been used. The device architecture is shown in Figure. 6a. and the I-V characteristics have been obtained for this device at dark conditions, shown in Figure. 6b. The Si/Ge I-V characteristics show a Schottky diode behavior with a cut-off potential of 0.47 V. The diode parameters are obtained from the semi-log plot of the I-V curve (Figure. 6c) and correlating with the ideal diode equations as given below,

$$I = I_o\left[\exp\left(\frac{qV}{nkT}\right) - 1\right] \tag{2.1}$$

$$I_o = AA^*T^2 \exp\left(\frac{-q\Phi_b}{kT}\right) \tag{2.2}$$

where q is electronic charge, k is the Boltzmann constant, T is the temperature, n is the diode ideality factor, I_o the reverse saturation current, A is the active device area (5 mm x 5 mm), A^* is the effective Richardson constant (143 A cm^{-2} K^{-2}) [55], Φ_b is the barrier height. The barrier height value of 0.83 eV has been obtained from equation 2.2. This value of barrier height is in accordance with the literature reports (~0.75 eV) [56, 57].

The slope of the semi-log plot determines the diode ideality factor and is found to be 5.1. Ideality of the diode is a way of determining, how well the charge transport mechanism could be described by the ideal diode equation. Ideality factor of 1 is estimated based on the assumptions such as band-to-band transitions or trap states lead to recombination. However, diodes possessing ideality factor of 1-2 is practically possible and hence η of values less than 2 is considered as ideal behavior. η value greater than 2 suggests that the diode is acted upon by several factors such as recombination, oxide layer, interface trap states and several phenomena [58-63]. In this work, the ideality diode factor of ~5.1 is observed. The ideality factor of the

diode depends on the heterogeneity and film porosity and also on several external factors such as the contact between the film and the electrode, the saturation current, the series resistance, the shunt conductance and the photocurrent. These parameters not only depend on the quality of the film but also on the preparation of the contacts [61, 64, 65]. The current experiments are performed to demonstrate the possibility of fabricating a diode using a simpler process and hence contact parameters are not optimized which reflect in the higher ideality factor of the fabricated heterostructures. The higher ideality factor shows that the diode behavior can no longer be understood based on only thermionic emission theory. This indicates that the current transport mechanism in these structures deviates from that of thermionic emission theory [66-68].

Hence, to probe the possible charge transport mechanisms, the log-log plot of the I-V curve has been obtained and is shown in Figure. 6d [69]. The log-log plot shows the power law compliance of the current with voltage. The plot shows four regions with distinct slopes. The slopes indicate a fit between current and voltage given by $I = KV^m$ [66, 70], where K is a constant and m is the exponent obtained from the slope of the curve. The first region is the Ohmic region, where the current varies linearly (m=1) with respect to the voltage. This trend is from Ohm's law behavior, where the charge transport is because of the thermally generated carriers. This happens during the initial stage, where the charge carriers because of the external biasing are small. Following this, region-II with a slope of about 2.3 appears. This region of space charge limited current (SCLC) starts, when the thermally generated charge carriers are comparable to the charge carriers injected due to biasing. In this region, the injected charge carriers fill the effective traps in the diode. Following this there is a sharp increase in the current flow, where the slope is high (m=4), which is the transition from the trap-filling region to the trap-free region. In the Si/Ge diode, this appears at the voltage of about 0.4 V. This is in correspondence with the cut-in

potential of the diode (0.47 V). After, this region, the injected carriers directly reach the conduction band (m=2.1). This elucidates that the inkjet-printed Si/Ge diode shows the space-charge-limited current transport behavior.

4 Conclusions

A cost-effective route to synthesize germanium nanoparticles through cryomilling is developed. Synthesis of germanium colloids in low boiling point solvents has also been achieved in this study, by functionalizing germanium nanoparticles with acrylic acid. This step provides oxide-stable propionic acid moiety terminated germanium colloid. Inkjet printing of germanium nanoparticles on silicon has been explored in further. The major issue of coffee-ring formation has been suppressed and Ge film on Si substrate with uniform morphology was obtained. Germanium film is achieved at ambient conditions, without the use of conventional vacuum fabrication technologies. Si/Ge heterojunction shows Schottky diode characteristics. This study paves the way for utilization of germanium in printable electronics.

Acknowledgements

This work is supported by part under the US– India Partnership to Advance Clean Energy-Research (PACE-R) for the Solar Energy Research Institute for India and the United States (SERIIUS), funded jointly by the U.S. Department of Energy (Office of Science, Office of Basic Energy Sciences, and Energy Efficiency and Renewable Energy, Solar Energy Technology Program, under Subcontract DE-AC36-08GO28308 to the National Renewable Energy Laboratory, Golden, Colorado) and the Government of India, through the Department of Science and Technology under Subcontract IUSSTF/JCERDC-SERIIUS/ 2012 dated 22nd Nov. 2012. The facilities provided by AFMM center and CeNSE at Indian Institute of Science are gratefully acknowledged.

References

[1] M. Wolf, R. Brendel, J.H. Werner, H.J. Queisser, Solar cell efficiency and carrier multiplication in Si(1-x)Ge(x) alloys, J Appl Phys 83(8) (1998) 4213-4221.

[2] W.G. Pan, K. Fujiwara, N. Usami, T. Ujihara, K. Nakajima, R. Shimokawa, Ge composition dependence of properties of solar cells based on multicrystalline SiGe with microscopic compositional distribution, J Appl Phys 96(2) (2004) 1238-1241.

[3] R.P.G. Karunasiri, J.S. Park, K.L. Wang, $Si_{1-X}Ge_x$/Si Multiple Quantum-Well Infrared Detector, Appl Phys Lett 59(20) (1991) 2588-2590.

[4] Z.H. Huang, C. Li, D. Liang, K.Z. Yu, C. Santori, M. Fiorentino, W. Sorin, S. Palermo, R.G. Beausoleil, 25 Gbps low-voltage waveguide Si-Ge avalanche photodiode, Optica 3(8) (2016) 793-798.

[5] E. Kasper, H.J. Herzog, H. Kibbel, A one-dimensional SiGe superlattice grown by UHV epitaxy, Applied physics 8(3) (1975) 199-205.

[6] S. Raman, P. Sharma, T.G. Neogi, M.R. LeRoy, R. Clarke, J.F. McDonald, On the Performance of Lateral SiGe Heterojunction Bipolar Transistors With Partially Depleted Base, IEEE T Electron Dev 62(8) (2015) 2377-2383.

[7] K. Ismail, Si/SiGe high-speed field-effect transistors, International Electron Devices Meeting, 1995 - Iedm Technical Digest (1995) 509-512.

[8] T.E. Whall, E.H.C. Parker, SiGe heterostructures for FET applications, J Phys D 31(12) (1998) 1397-1416.

[9] M. Ben Ishai, F. Patolsky, Shape- and Dimension-Controlled Single-Crystalline Silicon and SiGe Nanotubes: Toward Nanofluidic FET Devices, J Am Chem Soc 131(10) (2009) 3679-3689.

[10] A.I. Boukai, Y. Bunimovich, J. Tahir-Kheli, J.K. Yu, W.A. Goddard, J.R. Heath, Silicon nanowires as efficient thermoelectric materials, Nature 451(7175) (2008) 168-171.

[11] A. Samarelli, L.F. Llin, S. Cecchi, J. Frigerio, D. Chrastina, G. Isella, E.M. Gubler, T. Etzelstorfer, J. Stangl, Y. Zhang, J.M.R. Weaver, P.S. Dobson, D.J. Paul, Prospects for SiGe thermoelectric generators, Solid State Electron 98 (2014) 70-74.

[12] Y.X. Li, J. Han, Q.P. Xiang, C.F. Zhang, J. Li, Enhancing thermoelectric properties of p-type SiGe by SiMo addition, Journal of Materials Science-Materials in Electronics 30(10) (2019) 9163-9170.

[13] G.A.A. C.K Maiti, Applications of Silicon-Germanium Heterostructure Devices, CRC Press2001.

[14] M. Singh, H.M. Haverinen, P. Dhagat, G.E. Jabbour, Inkjet Printing-Process and Its Applications, Adv Mater 22(6) (2010) 673-685.

[15] E. Drahi, A. Gupta, S. Blayac, S. Saunier, P. Benaben, Characterization of sintered inkjet-printed silicon nanoparticle thin films for thermoelectric devices, Physica Status Solidi a-Applications and Materials Science 211(6) (2014) 1301-1307.

[16] N. Marjanovic, A. Chiolerio, M. Kus, F. Ozel, S. Tilki, N. Ivanovic, Z. Rakocevic, V. Andric, T. Barudzija, R.R. Baumann, Magnetite nanoparticles: Synthesis, thin film properties

and inkjet printing of magnetic cores for inductor applications, Thin Solid Films 570 (2014) 38-44.

[17] D. Stuwe, D. Mager, D. Biro, J.G. Korvink, Inkjet Technology for Crystalline Silicon Photovoltaics, Adv Mater 27(4) (2015) 599-626.

[18] R. Gresback, Z. Holman, U. Kortshagen, Nonthermal plasma synthesis of size-controlled, monodisperse, freestanding germanium nanocrystals, Appl Phys Lett 91 (2007) 093119.

[19] C.-S. Yang, R.A. Bley, S.M. Kauzlarich, H.W.H. Lee, G.R. Delgado, Synthesis of Alkyl-Terminated Silicon Nanoclusters by a Solution Route, J Am Chem Soc 121 (1999) 5191-5195.

[20] S.C. Codoluto, W.J. Baumgardner, T. Hanrath, Fundamental aspects of nucleation and growth in the solution-phase synthesis of germanium nanocrystals, 12 (2010) 2903-2909.

[21] S. Vadava, S. Valligatla, B. Neelamraju, M.H. Dar, A. Chiasera, M. Ferrari, N.R. Desai, Optical properties of germanium nanoparticles synthesized by pulsed laser ablation in acetone, Frontiers in Physics 2 (2014).

[22] E.J. Henderson, M. Seino, D.P. Puzzo, G.A. Ozin, Colloidally Stable Germanium Nanocrystals for Photonic Applications, ACS Nano 4 (2010) 7683-7691.

[23] C.S. Tiwary, R.J. Mudakavi, S. Kishore, S. Kashyap, R. Elumalai, D. Chakravortty, A.M. Raichur, K. Chattopadhyay, Magnetic iron nanoparticles for in vivo targeted delivery and as biocompatible contrast agents, Rsc Adv 6 (2016) 114344-114352.

[24] C.S. Tiwary, S. Kashyap, K. Biswas, K. Chattopadhyay, Synthesis of Pure Iron Magnetic Nanoparticles in Large Quantity, J PHYS D APPL PHYS 46 (2013) 385001.

[25] A. Albrecht, M. Bobinger, J.F. Salmeron, M. Becherer, G. Cheng, P. Lugli, A. Rivadeneyra, Over-Stretching Tolerant Conductors on Rubber Films by Inkjet-Printing Silver Nanoparticles for Wearables, Polymers 10(12) (2018).

[26] G. Perçin, T.S. Lundgren, B.T. Khuri-Yakub, Controlled ink-jet printing and deposition of organic polymers and solid particles, Appl Phys Lett 73(16) (1998) 2375-2377.

[27] D. Kim, S. Jeong, S. Lee, B.K. Park, J. Moon, Organic thin film transistor using silver electrodes by the ink-jet printing technology, Thin Solid Films 515(19) (2007) 7692-7696.

[28] D.Y. Shin, P.J. Smith, Theoretical investigation of the influence of nozzle diameter variation on the fabrication of thin film transistor liquid crystal display color filters, J Appl Phys 103(11) (2008).

[29] J. Vukmirovic, D. Tripkovic, B. Bajac, S. Kojic, G.M. Stojanovic, V.V. Srdic, Comparison of barium titanate thin films prepared by inkjet printing and spin coating, Processing and Application of Ceramics 9(3) (2015) 151-156.

[30] D. Tripkovic, J. Vukmirovic, B. Bajac, N. Samardzic, E. Djurdjic, G. Stojanovic, V.V. Srdic, Inkjet patterning of in situ sol-gel derived barium titanate thin films, Ceramics International 42(1) (2016) 1840-1846.

[31] K.T. Park, H.J. Kim, M.J. Park, J.H. Jeong, J. Lee, D.G. Choi, J.H. Lee, J.H. Choi, 13.2% efficiency Si nanowire/PEDOT:PSS hybrid solar cell using a transfer-imprinted Au mesh electrode, Scientific Reports 5 (2015).

[32] A. Haldar, K.S. Liao, S.A. Curran, Effect of printing parameters and annealing on organic photovoltaics performance, J Mater Res 27(16) (2012) 2079-2087.

[33] C.E. Finlayson, A. Amezcua-Correa, P.J.A. Sazio, N.F. Baril, J.V. Badding, Electrical and Raman characterization of silicon and germanium-filled microstructured optical fibers, Appl Phys Lett 90(13) (2007).

[34] N.J. Welham, Formation and characterization of germanium nanoparticles, J Mater Res 15 (2000) 2400-2407.

[35] J.P. Wilcoxon, P.P. Provencio, G.A. Samara, Synthesis and optical properties of colloidal germanium nanocrystals, Phys Rev B 64(3) (2001).

[36] E. Gaffet, Phase transition induced by ball milling in germanium, Mater Sci Eng A 136 (1991) 161–169.

[37] E. Gaffet, F. Faudot, M. Harmelin, Crystal-to-Amorphous Phase-Transition Induced by Mechanical Alloying in the Ge-Si System, Materials Science and Engineering a-Structural Materials Properties Microstructure and Processing 149(1) (1991) 85-94.

[38] E. Gaffet, F. Faudot, M. Harmelin, Amorphization Induced by Ball-Milling in Some Pure Elements - Si, Ge, Ordering and Disordering in Alloys1992, pp. 423-433.

[39] E. Gaffet, F. Faudot, M. Harmelin, Metastable Phase-Transition Induced by Ball-Milling in the Ge-Si System, Mater Sci Forum 88 (1992) 375-382.

[40] R. Bywalez, H. Karacuban, H. Nienhaus, C. Schulz, H. Wiggers, Stabilization of mid-sized silicon nanoparticles by functionalization with acrylic acid, Nanoscale Research Letters 7 (2012) 76.

[41] T.K. Purkait, A.K. Swarnakar, G.B. De Los Reyes, F.A. Hegmann, E. Rivard, J.G.C. Veinot, One-pot synthesis of functionalized germanium nanocrystals from a single source precursor, Nanoscale 7(6) (2015) 2241-2244.

[42] G. Collins, P. Fleming, C. O'Dwyer, M.A. Morris, J.D. Holmes, Functionalization of Germanium Nanowires, Ecs Transactions 35(8) (2011) 89-99.

[43] G. Collins, D. Aureau, J.D. Holmes, A. Etcheberry, C. O'Dwyer, Germanium Oxide Removal by Citric Acid and Thiol Passivation from Citric Acid-Terminated Ge(100), Langmuir 30(47) (2014) 14123-14127.

[44] S.Y. Lin, C.H. Chen, Y.C. Chan, C.M. Lin, H.W. Chen, Self-assembly of alkanoic acids on gold surfaces modified by underpotential deposition, J Phys Chem B 105(21) (2001) 4951-4955.

[45] B.R. Taylor, S.M. Kauzlarich, G.R. Delgado, H.W.H. Lee, Solution Synthesis and Characterization of Quantum Confined Ge Nanoparticles, Chem Mater 11 (1999) 2493-2500.

[46] S. Rivillon, Y.J. Chabal, F. Amy, A. Kahn, Hydrogen passivation of germanium (100) surface using wet chemical preparation, Appl Phys Lett 87(25) (2005).

[47] S. Sato, M.T. Swihart, Propionic-acid-terminated silicon nanoparticles: Synthesis and optical characterization, Chem Mater 18(17) (2006) 4083-4088.

[48] J.Z. Sun, M.X. Kuang, Y.L. Song, Control and Application of "Coffee Ring" Effect in Inkjet Printing, Prog Chem 27(8) (2015) 979-985.

[49] X.Y. Shen, C.M. Ho, T.S. Wong, Minimal Size of Coffee Ring Structure, J Phys Chem B 114(16) (2010) 5269-5274.

[50] D. Soltman, V. Subramanian, Inkjet-printed line morphologies and temperature control of the coffee ring effect, Langmuir 24(5) (2008) 2224-31.

[51] R.D. Deegan, O. Bakajin, T.F. Dupont, G. Huber, S.R. Nagel, T.A. Witten, Capillary flow as the cause of ring stains from dried liquid drops, Nature 389(6653) (1997) 827-829.

[52] K. Chattopadhyay, R. Goswami, Melting and superheating of metals and alloys, Prog Mater Sci 42(1-4) (1997) 287-300.

[53] R. Goswami, K. Chattopadhyay, Melting of Bi nanoparticles embedded in a Zn matrix, Acta Mater 52(19) (2004) 5503-5510.

[54] G.X. Cheng, H. Xia, K.J. Chen, W. Zhang, X.K. Zhang, Raman Measurement of the Grain-Size for Silicon Crystallites, Physica Status Solidi a-Applied Research 118(1) (1990) K51-K54.

[55] Z.Q. Li, X. An, Q.X. Yun, M. Lin, X. Zhang, R. Huang, Tuning Schottky Barrier Height in Metal/n-Type Germanium by Inserting an Ultrathin Yttrium Oxide Film, Ecs Solid State Letters 1(4) (2012) Q33-Q34.

[56] R. Balsano, A. Matsubayashi, V.P. LaBella, Schottky barrier height measurements of Cu/Si(001), Ag/Si(001), and Au/Si(001) interfaces utilizing ballistic electron emission microscopy and ballistic hole emission microscopy, Aip Advances 3(11) (2013).

[57] H.H. Weitering, J.P. Sullivan, R.J. Carolissen, R. PerezSandoz, W.R. Graham, R.T. Tung, Inhomogeneous Schottky barriers at Ag/Si(111) and Ag/Si(100) interfaces, J Appl Phys 79(10) (1996) 7820-7829.

[58] C.T. Sah, R.N. Noyce, W. Shockley, Carrier Generation and Recombination in P-N Junctions and P-N Junction Characteristics, Proc Inst Radio Eng 45(9) (1957) 1228-1243.

[59] M. Tyagi, M. Tomar, V. Gupta, Trap Assisted Space Charge Conduction in p-NiO/n-ZnO Heterojunction Diode, Mater Res Bull 66 (2015) 123-131.

[60] D. Zhu, J.R. Xu, A.N. Noemaun, J.K. Kim, E.F. Schubert, M.H. Crawford, D.D. Koleske, The Origin of the High Diode-Ideality Factors in GaInN/GaN Multiple Quantum Well Light-Emitting Diodes, Appl Phys Lett 94(8) (2009).

[61] C.X. Wang, G.W. Yang, H.W. Liu, Y.H. Han, J.F. Luo, C.X. Gao, G.T. Zou, Experimental Analysis and Theoretical Model for Anomalously High Ideality Factors in ZnO/Diamond p-n Junction Diode, Appl Phys Lett 84(13) (2004) 2427-2429.

[62] J.M. Shah, Y.L. Li, T. Gessmann, E.F. Schubert, Experimental Analysis and a New Theoretical Model for Anomalously High Ideality Factors (n >> 2.0) in AlGaN/GaN p-n Junction Diodes, J Appl Phys 798 (2003) 113-118.

[63] H.C. Casey, J. Muth, S. Krishnankutty, J.M. Zavada, Dominance of Tunneling Current and Band Filling in InGaN/AlGaN Double Heterostructure Blue Light-Emitting Diodes, Appl Phys Lett 68(20) (1996) 2867-2869.

[64] C.H. Belgacem, A.A. El-Amine, Theoretical Models for Anomalously High Ideality Factor in a Au/SnO2-Si(n)/Al Solar Cell, Silicon-Neth 10(3) (2018) 1063-1066.

[65] V. Cahill, D. Taylor, Evaluation of Inkjet Technologies for Digital Fabrication & Functional Printing, Nip28: 28th International Conference on Digital Printing Technologies / Digital Fabrication 2012 (2012) 315-317.

[66] P.C. Ramamurthy, W.R. Harrell, R.V. Gregory, B. Sadanadan, A.M. Rao, Polyaniline/Carbon Nanotube Composite Schottky Contacts, Polym Eng Sci 44(1) (2004) 28-33.

[67] P.C. Ramamurthy, A.M. Malshe, W.R. Harrell, R.V. Gregory, K. McGuire, A.M. Rao, Polyaniline/Single-Walled Carbon Nanotube Composite Electronic Devices, Solid State Electron 48(10-11) (2004) 2019-2024.

[68] P.C. Ramamurthy, A.M. Malshe, W.R. Harrell, R.V. Gregory, K. McGuire, A.M. Rao, Electronic Device Fabricated from Polyaniline/Single Walled Carbon Nanotubes Composite, Mater Res Soc Symp Proc 772 (2003) 217-222.

[69] P. Singh, P.K. Rout, H. Pandey, A. Dogra, Temperature-Dependent Space-Charge-Limited Conduction in $BaTiO_3$ Heterojunctions, J Mater Sci 53(7) (2018) 4806-4813.

[70] X. Qiao, J. Chen, D. Ma, Trap-Free Space-Charge-Limited Electron Transport in Amorphous tin(IV) phthalocyanine dichloride Thin Film, J Phys D 43 (2010) 215402.

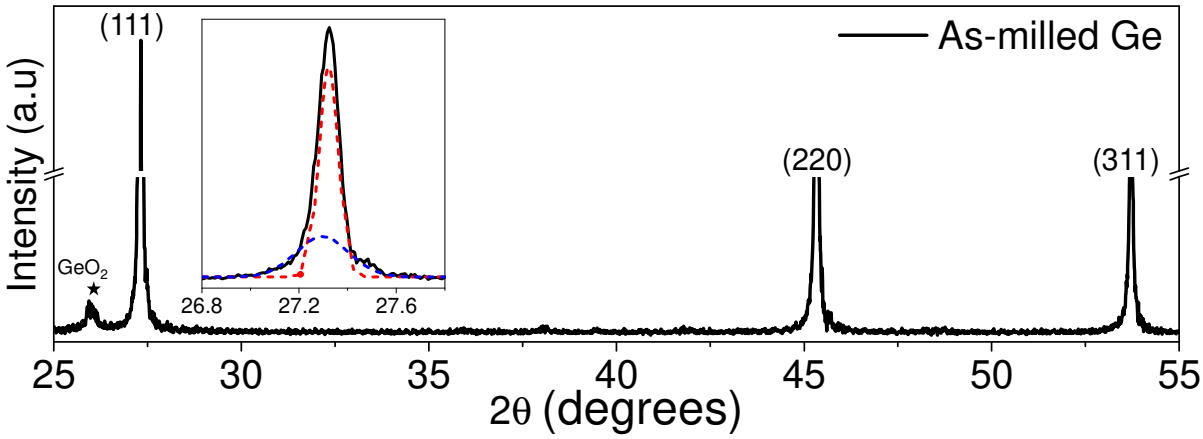

Figure. 1. XRD pattern of the cryomilled germanium powder. The peaks correspond to the diamond cubic structure of the germanium and shows the presence of small amount of germanium oxide. The inset shows the deconvoluted peak of (111) plane where the broadened peak corresponds to a finer crystallite size of ~50 nm.

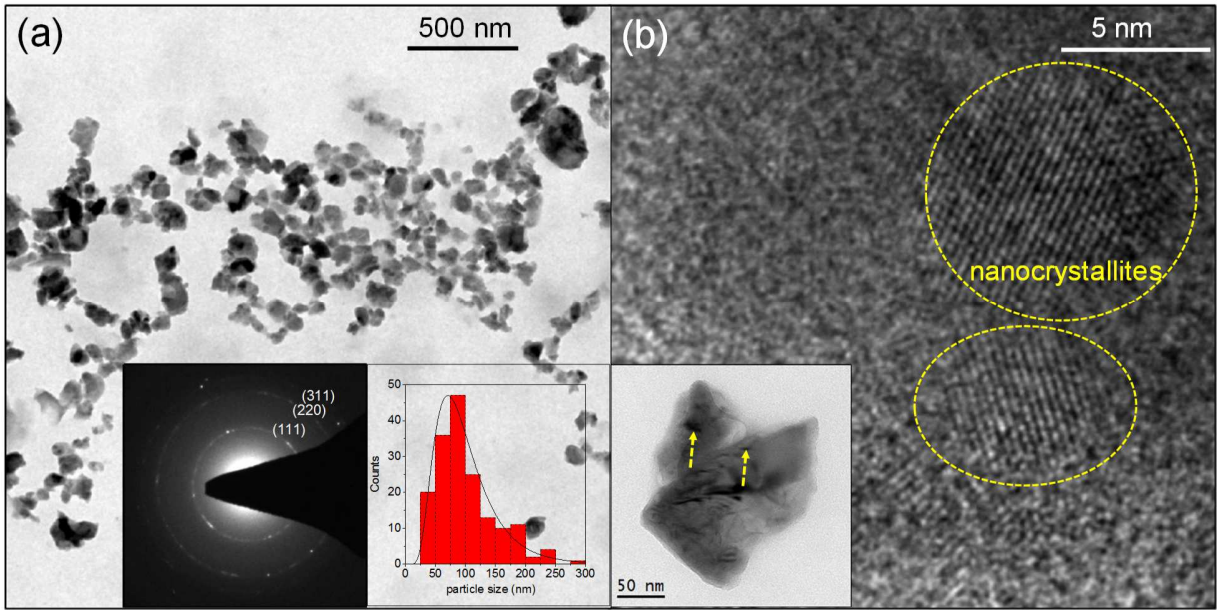

Figure. 2. a) TEM micrograph of the Ge NPs, inset showing the corresponding diffraction pattern indicating the diamond cubic Ge structure. Size distribution of the particles with mode at 80 nm as shown in the inset. b) High Resolution TEM image of the partiles showing the presence of nanocrystallites. Inset showing the individual particle with diffraction **contrast** indicative of crystalllites showing nanocrystallites in the particle.

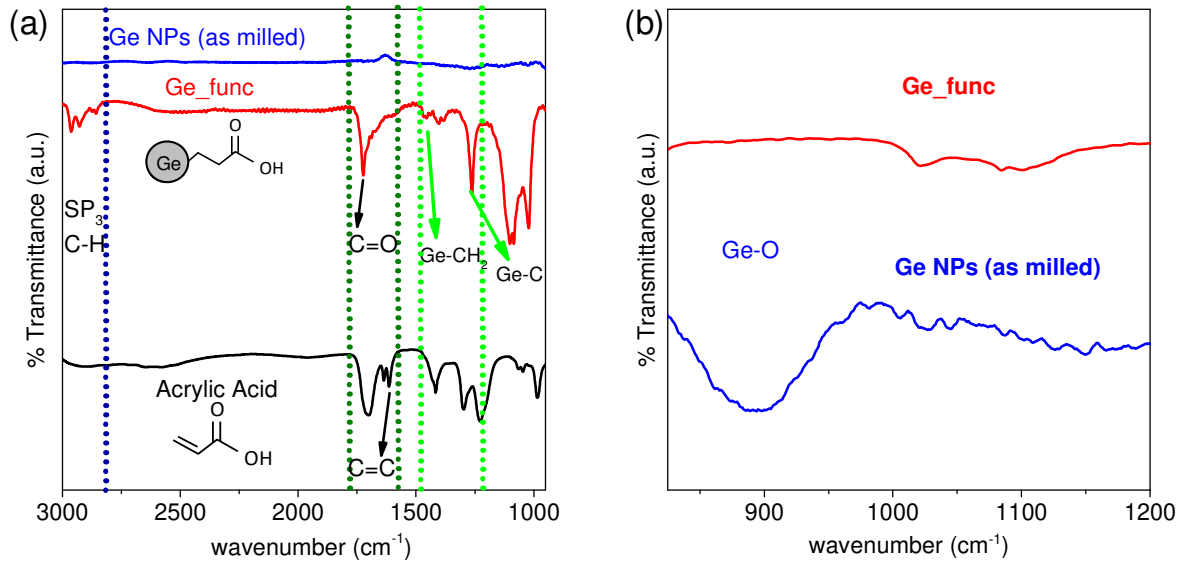

Figure. 3. a) FTIR spectra of the as-milled Ge NPs, functionalized Ge NPs indicated as 'Ge_func' and acrylic acid. b) Magnified view of the FTIR spectra showing the disappearance of oxide peaks in functionalized germanium nanoparticles.

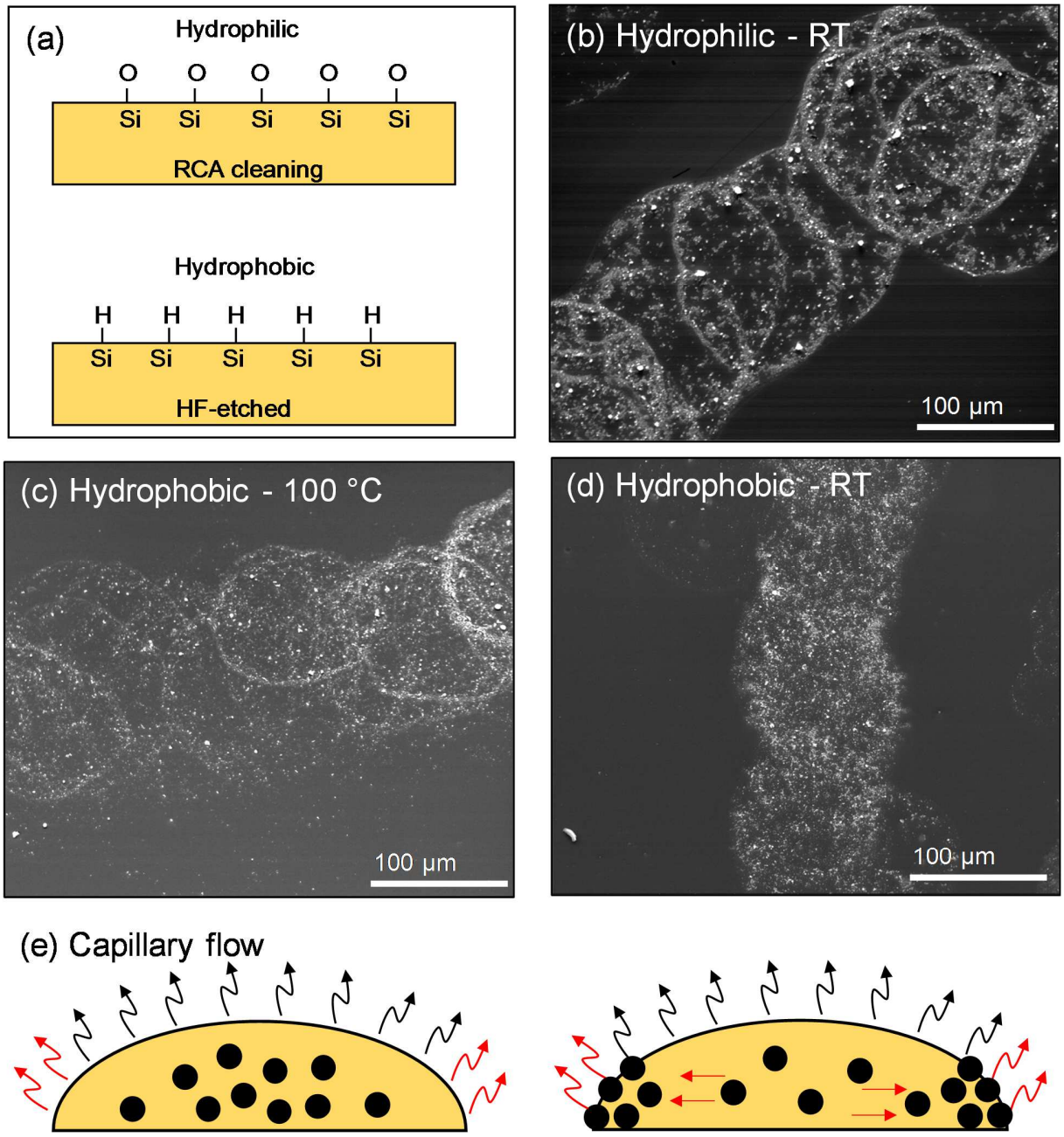

Figure. 4. a) Oxide-termination of the Si wafer after the RCA cleaning process making the surface hydrophilic and HF-etching results in hydrogen termination of the Si surface leading to hydrophobicity. b) Morphology of the drops formed on a hydrophilic surface showing the prominent coffee ring formation. c) Morphology of the drop on the hydrophobic surface printed at 100 °C showing the presence of coffee-ring. d) Morphology of the drop on hydrophobic surface printed at room temperature showing uniform morphology. e) Schematic of the capillary flow, showing the segregation of the particles in the periphery due to faster evaporation of solvent in the periphery (indicated by red arrows).

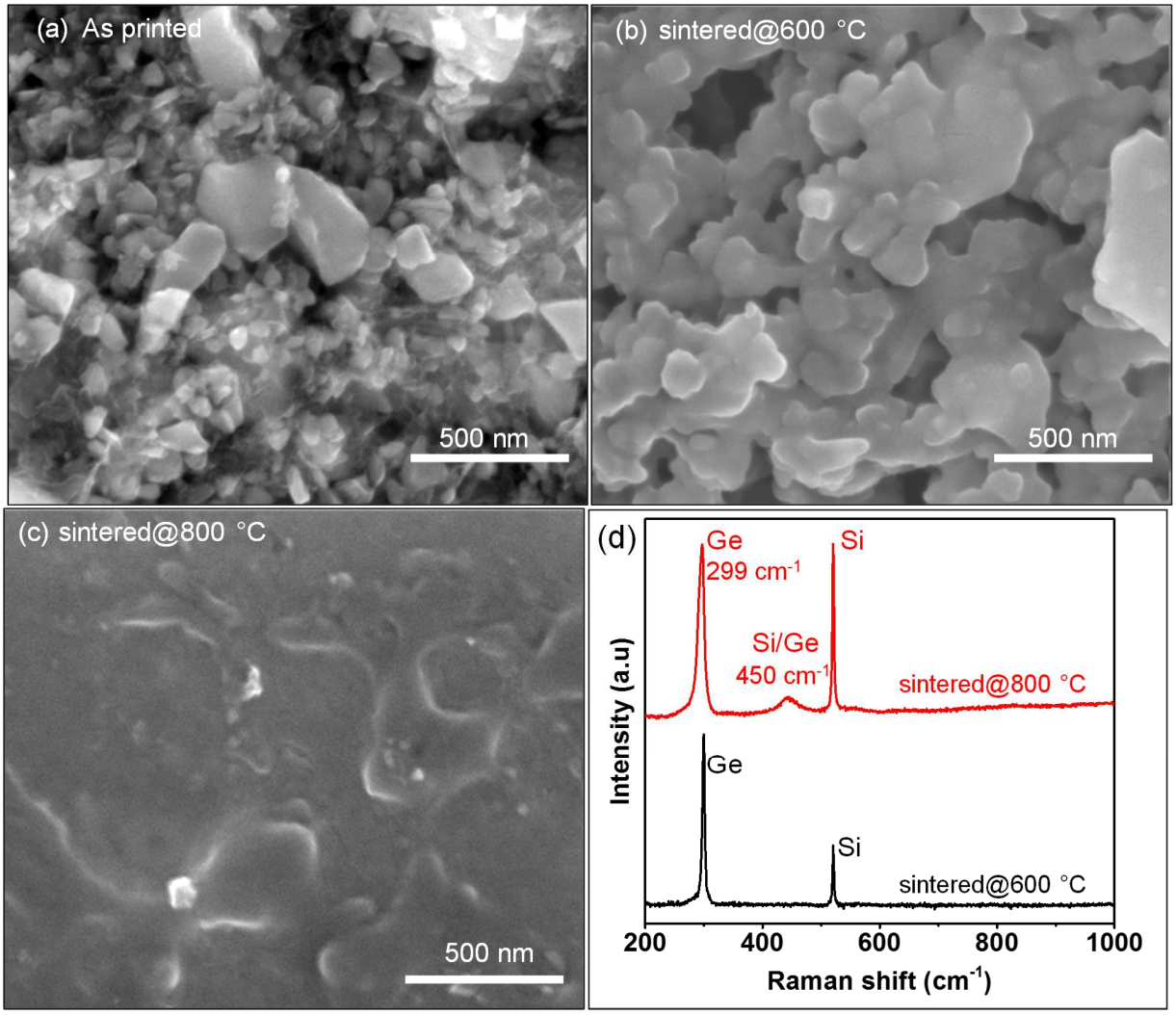

Figure. 5. a) Morphology of the functionalized Ge dispersed in IPA, printed on hydrophobic Si substrate with substrate temperature maintained at room temperature. Samples sintered under vacuum at b) 600 °C for 1.5 hr showing the initiation of sintering and c) 800 °C for 2.5 hr showing the uniform morphology in the film, due to the melting of the particles. d) Raman spectra for the germanium films obtained by sintering at 600 °C and 800 °C.

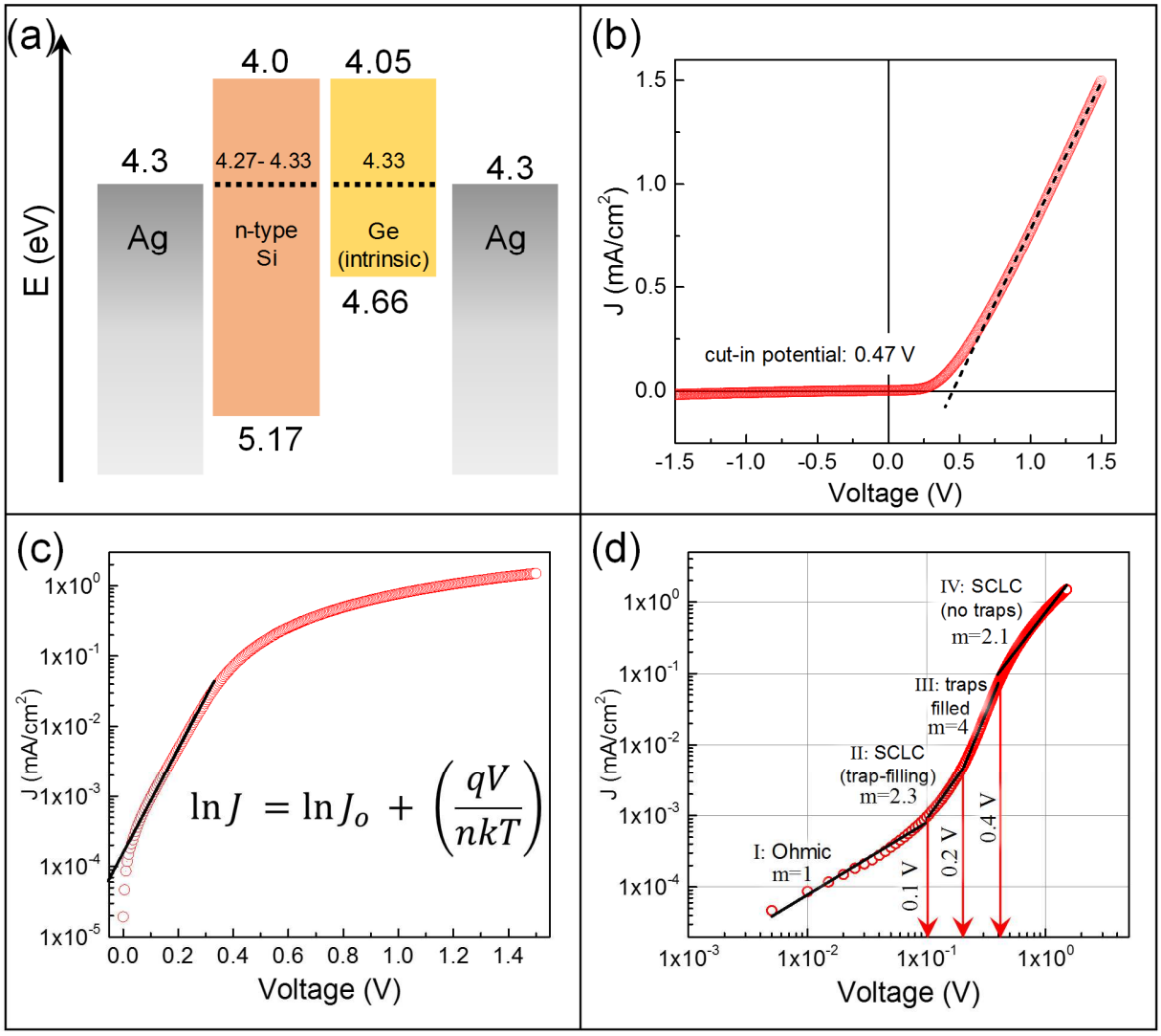

Figure. 6. a) Device architecture used for measuring the current-voltage response in the inkjet printed Si/Ge heterostructure. b) J-V plot showing the schottky diode behavior with a cut-in potential ojf 0.47 V. c) Semi-log plot to measure the diode parameters, inset showing the ideal diode equation d) Power plot showing the space charge limited current conduction in the Si/Ge heterojunction.

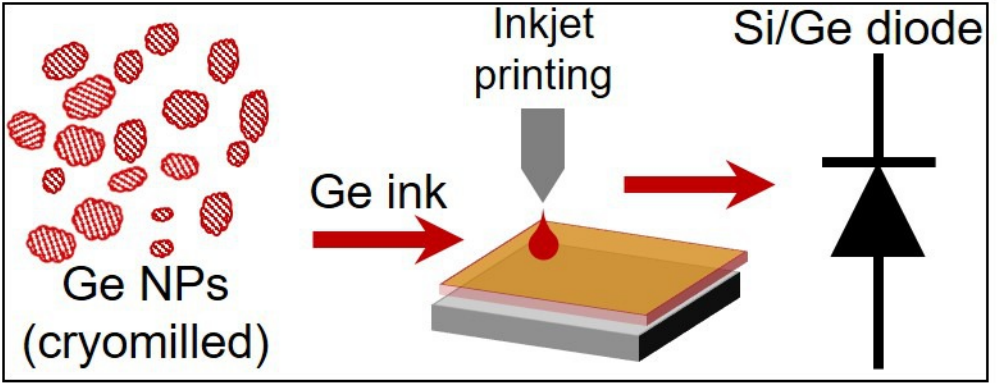
Inkjet
printing
Si/Ge diode
Ge ink
Ge NPs
(cryomilled)